Chapter 4

PHOTON-NUMBER-RESOLVING SUPERCONDUCTING NANOWIRE ARRAY DETECTORS

This chapter includes the work in preparation for publication:

[1] Samantha I. Davis, Prathwiraj Umesh, Ioana Craiciu, Raju Valivarthi, Boris Korzh, Matthew Shaw, and Maria Spiropulu. "Photon number resolution with superconducting nanowire arrays." In: Manuscript in preparation. (2025).

4.1 Introduction

Photon-number-resolving detectors (PNRDs) are indispensable for a wide range of quantum technologies, including linear-optical quantum computing, quantum key distribution and quantum metrology. Transition-edge sensors (TESs), microwave kinetic-inductance detectors (MKIDs), and superconducting nanowire single-photon detectors (SNSPDs) already deliver high efficiencies and sub-nanosecond timing, yet their intrinsic photon number resolution eventually saturates as incident photon flux increases, limiting dynamic range [1, 2, 3]. Pseudo-PNR schemes based on temporal, spatial or spectral multiplexing circumvent this ceiling by distributing photons over many modes and reading them out with threshold detectors [4, 5]. Parallel advances in nanofabrication now enable dense on-chip integration of hundreds of SNSPD pixels and sophisticated fan-out architectures [6, 7, 8]. There are therefore two types of PNR detection: (1) intrinsic PNR where a single detector is sensitive to the energy difference between one, two, or more photons being absorbed in a short time window, (2) pseudo-PNR, where incoming photons are distributed over multiple spatial or temporal modes before being detected. The two types can be combined, for example by an array of intrinsic-PNRDs, or combining one intrinsic-PNRD with temporal multiplexing. Merging the advances in multiplexing with single-pixel photon number resolution charts a practical route toward the ideal, high-dynamic-range PNRD.

The quantitative behaviour of a PNRD is fully specified by its positive-operator-valued measure (POVM). Closed-form solutions for POVM elements are known for the case of uniform splitting probabilities across an array of click detectors [9], relevant to spatially and temporally mulitplexed pseudo-PNRDs [4, 5]. Uniform-splitting

assumptions, however, break down in large-scale array detectors [10, 11] where spatial-mode weights are inherently non-uniform and pixel-to-pixel efficiencies vary because of optical coupling and fabrication tolerances. A general treatment requires a multinomial expansion over all detector outcomes whose term count grows exponentially with array size, rendering brute-force evaluation intractable for state-of-the-art devices. No analytic solution has yet been reported for this non-uniform regime. More broadly, a model for the POVM elements of detector arrays with arbitrary POVMs is needed to support the development of scalable architectures composed of photon-number-resolving detectors.

Here we close this gap by developing a generalized theoretical framework for POVM modeling of realistic PNR detector arrays. First we present a model for an array of detectors with arbitrary POVMs and splitting topologies. We find a closed-form solution for case of click detectors and non-uniform splitting probabilities, and present an iterative method for efficiently constructing the POVM of an array detector from known detector POVMs and splitting probabilities. Next, we validate the model by experimentally reconstructing the POVMs of two detector configurations: (1) a pseudo-PNR array of threshold detectors with heterogeneous splitting probabilities–an architecture exemplified by recent developments in SNSPD detector arrays [10, 11], and (2) an array of six intrinsic-PNRDs. We perform experimental detector tomography of (1) the PEACOQ detector from Ref. [10] and (2) a spatially-mutliplexed array of six PNR SNSPDs to demonstrate configurations 1 and 2, respectively. These two experimental demonstrations showcase our modeling framework as a practical toolset for designing and optimizing next-generation PNR arrays, which will advance the broader quest for detectors that approach the ideal photon-number-resolving limit.

4.2 Generalized POVM model for array detectors

In quantum optics, the measurement statistics of a single-photon detector are fully characterized by a set of positive operator value measure (POVM) elements $\{\hat{\pi}_n\}$, where each $\hat{\pi}_m$ is a positive semi-definite operator associated with the outcome m. For an input state ρ, the probability of observing outcome m is given by,

$$p_m = \mathrm{Tr}[\rho\hat{\pi}_m]. \tag{4.1}$$

The POVM elements can be expanded in a complete basis over any Hilbert space. Relevant to photon-number-resolving detection, under the assumption that the detector is insensitive to the phase of the input light, the POVM elements can be

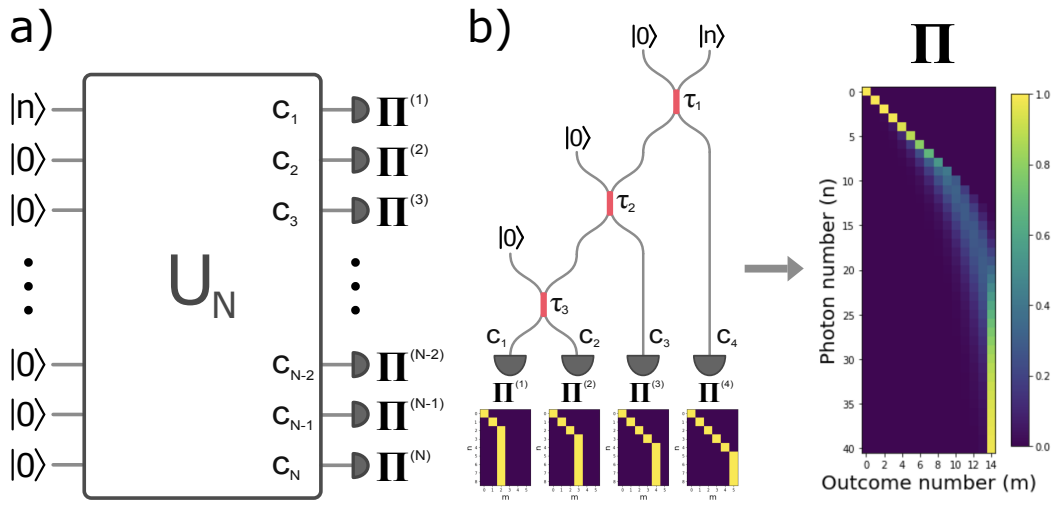

Figure 4.1: Setup for theoretical modeling. a) An n-photon number state, $|n\rangle$, is injected into the first input port of a $2N$-port beamsplitter, described by the unitary operator U_N. The n photons are distributed across a set of N detectors, where c_k is the splitting amplitude for the kth output port and $\mathbf{\Pi}^{(k)}$ is the conditional probability matrix of the kth detector. b) Conceptual illustration of POVM construction from an array of detectors with different photon number resolving capabilities. $\mathbf{\Pi}^{(n)}$ is the conditional probability matrix for the nth detector $\mathbf{\Pi}$ is the conditional probability matrix for the overall array of multiplexed detectors.

expressed in the photon number basis as,

$$\hat{\pi}_m = \sum_{n=0}^{\infty} P(m|n)\,|n\rangle\langle n| = \sum_{n=0}^{\infty} \mathbf{\Pi}_{m,n}\,|n\rangle\langle n|\,, \tag{4.2}$$

where $P(m|n)$ is the conditional probability that the detector outputs outcome m given n input photons and $|n\rangle$ is the photon number state of n photons. In this notation, the POVM of a detector can be completely summarized by the conditional probability matrix $\hat{\Pi}$, with matrix elements $\mathbf{\Pi}_{m,n} = P(m|n)$. For an ideal photon-number-resolving detector, the POVM elements are $\{\hat{\pi}_n = |n\rangle\langle n|\}$ and the conditional probability matrix is the identity matrix, $\mathbf{\Pi}_{mn} = \delta_{mn}$. In practice, the photon number resolution of a realistic detector saturates, with photon resolution demonstrated up to 15 photons at 1550 nm with single TES detector [12], resulting in a truncated number of measurement outcomes. In turn, this limits the dynamic range of a detector up to the photon number saturation.

Multiplexing is a common approach to overcoming photon number saturation, whereby n photons are distributed over a set of spatial [9], temporal [4, 5], or

spectral modes such that a smaller number of photons are incident to the detector at each mode. The splitting operation can be modeled using linear optics as a $2N$-port beamsplitter with an associated unitary operator U_N, where N is the number of input and output modes (see Fig. 4.1a). A photon number state $|n\rangle$ inserted into one of the input modes, with all others in the vacuum state. The photons are distributed to a set of N detectors, one at each output mode, where c_k represents the probability of a single photon arriving to output mode $k \in \{1, ..., N\}$ ("splitting probability"). Each detector has a set of POVM elements $\{\hat{\pi}_n^{(k)}\}$, where the POVM elements of the detector at output mode k are described by the conditional probability matrix $\mathbf{\Pi}^{(k)}$. The measurement outcomes of the multiplexed detector are found by summing the measurement outcomes of each detector. Let $\mathbf{\Pi}$ denote the conditional probability matrix of the multiplexed detector. The matrix element $\mathbf{\Pi}_{mn}$ corresponding to the mth measurement outcome given n input photons is,

$$\mathbf{\Pi}_{mn} = \sum_{\{\sum_k m_k = m\}} \sum_{\{\sum_k j_k = n\}} \frac{n!}{j_1! \cdots j_N!} c_1^{j_1} \cdots c_N^{j_N} \mathbf{\Pi}^{(1)}_{m_1 j_1} \cdots \mathbf{\Pi}^{(N)}_{m_N j_N}, \tag{4.3}$$

where the right hand side calculated as a multinomial expansion over the splitting probabilities $(c_1, ..., c_N)$, and individual detector matrices $(\mathbf{\Pi}^1, ..., \mathbf{\Pi}^N)$. In Eq. 4.3, the inner sum accounts for all possible ways n photons can be distributed over the N detectors, denoted as $\{\sum_k j_k = n\}$, where j_k is the number of photons incident to the kth detector. The outer sum accounts for each set of coincident photon number outcomes that sums to the measurement outcome m, denoted as $\{\sum_k m_k = m\}$, where m_k is the measured photon number by the kth detector.

Click detector arrays

For the case of click detection at each output, in which each detector can resolve either zero or at least one photon, the conditional probability matrix of the kth detector is given by,

$$\mathbf{\Pi}^{(k)} = \begin{pmatrix} 1 & 0 & \cdots & 0 \\ 0 & 1 & \cdots & 1 \end{pmatrix}, \tag{4.4}$$

where the first row corresponds to the detection of the vacuum state and the second row corresponds to the detection of at least one photon, interpreted as the measurement outcome of zero photons ($m_k = 0$) and one photon ($m_k = 1$), respectively.

In this case, Eq. 4.3 simplifies to [3],

$$\mathbf{\Pi}_{mn} = \sum_{\{\sum_k j_k = n\}}^{(m)} \frac{n!}{j_1! \cdots j_N!} c_1^{j_1} \cdots c_N^{j_N}, \tag{4.5}$$

where (m) denotes the condition that exactly m of $(j_1, ..., j_N)$ are nonzero. The number of terms in the sum of Eq. 4.5 scales polynomially in m and exponentially in n, which becomes computationally intractable for large n. To compute $\mathbf{\Pi}_{nm}$, a closed-form solution is desirable.

We obtain a closed-form expression by finding a recursion equation satisfied by the matrix elements in Eq. 4.5. Let $P(n, \vec{c}^{(m)})$ be the probability that n photons arrive to a subset of m wires, where $\vec{c}^{(m)}$ is the vector of probabilities for those m wires; there are $\binom{N}{m}$ such vectors, each of size m. We can rewrite $\mathbf{\Pi}_{m,n}$ as

$$\mathbf{\Pi}_{m,n} = \sum_{\vec{c}^{(m)}} P(n, \vec{c}^{(m)}) \tag{4.6}$$

where the sum is over all possible $\vec{c}^{(m)}$, i.e. over all possible subsets of m wires.

For a given subset of m wires, $P(n, \vec{c}^{(m)})$ obeys the recursion relation,

$$P(n, \vec{c}^{(m)}) = P(n-1, \vec{c}^{(m)}) \left(\sum_{k=1}^{m} \vec{c}_k^{(m)} \right) + \sum_{k=1}^{m} P(n-1, \vec{c}^{(m-1)}[k]) \vec{c}_k^{(m)} \tag{4.7}$$

where $\vec{c}_k^{(m)}$ is the kth element of $\vec{c}_k^{(m)}$ and $\vec{c}^{(m-1)}[k]$ is the subvector of $\vec{c}^{(m)}$ that excludes the element $\vec{c}_k^{(m)}$. The right hand side (RHS) accounts for the two cases of the nth photon arriving to the m wires: (1) the first term is the probability that the nth photon goes to one of the m wires given that $n-1$ photons already arrived to the m wires; (2) the second term is the probability the nth photon arrives to the kth wire given that $n-1$ photons already arrived to the other $m-1$ wires, summed over all $k = 1$ to $k = m$ wires.

The solution to the recursion relation yields (see Methods),

$$\mathbf{\Pi}_{m,n} = \binom{N}{m} \sum_{i=0}^{m} (-1)^i \frac{\binom{m}{i}}{\binom{N}{m-i}} \sum_{\vec{c}^{(m-i)}} \left(\sum_{k=1}^{m-i} \vec{c}_k^{(m-i)} \right)^n \tag{4.8}$$

where $\vec{c}^{(m-i)}$ is the vector of probabilities formed by removing a subset of i elements from $\vec{c}^{(m)}$; there are $\binom{N}{m-i}$ such vectors. The second sum in Eq. 4.8 is over all possible choices of $\vec{c}^{(m-i)}$. With Eq. 4.8, the number of terms is independent of n, providing an exponential improvement for large n in the computation of $\mathbf{\Pi}_{m,n}$ over the brute force computation using Eq. 4.5.

Without assumptions in the splitting probabilities, Eq. 4.8 is the most general closed-form solution for calculating the POVM elements of multiplexed threshold detector arrays. The scaling in N and m can be further improved leveraging symmetries in

$\vec{c}$. In the case of uniform splitting probabilities ($c_j = 1/N$ for $j = 1, ..., N$), Eq. 4.8 simplifies to the commonly used expression [9],

$$\mathbf{\Pi}_{mn} = \frac{m!}{N^n}\binom{N}{m} S(n, m), \quad N \geq n \geq m, \tag{4.9}$$

where $S(n, m) = \frac{1}{m!}\sum_{i=0}^{m}(-1)^i\binom{m}{i}(m-i)^n$ is the Stirling number of the second kind, that is, the number of ways of partitioning a set of n elements into exactly m non-empty subsets.

Detector arrays with arbitrary POVMs: iterative construction

Next, we consider the general case of Eq. 4.3 for an array of detectors with arbitrary POVMs. For the simplest case of two detectors with splitting probabilities $\vec{c} = (c_1, c_2)$, which corresponds to a 2-port beamsplitter with transmittance τ where $c_1 = |\tau|^2$ and $c_2 = 1 - |\tau|^2$, the conditional probability matrix is,

$$\mathbf{\Pi}_{mn} = \sum_{i=0}^{m}\sum_{j=0}^{n}\binom{n}{j}(c_1)^j(c_2)^{n-j}\mathbf{\Pi}^{(1)}_{i,j}\mathbf{\Pi}^{(2)}_{m-i,n-j}, \tag{4.10}$$

where $\mathbf{\Pi}^{(k)}$ and $\mathbf{\Pi}^{(2)}$ are the conditional probability matrices of detectors 1 and 2, respectively.

The $\mathbf{\Pi}$ matrix of an array of N detectors can be iteratively constructed by pairing subsets of detectors using Eq. 4.10. The N splitting probabilities $\vec{c} = (c_1, c_2, ...c_n)$ can be mapped to a $2N$-port beamsplitter comprised of $N - 1$ beamsplitters with transmittances $\vec{\tau} = (\tau_1, \tau_2, ...\tau_{N-1})$ (see Methods). The iterative construction is illustrated in Fig. 4.1b for an array of four detectors. The heat maps for the conditional probability matrices $\mathbf{\Pi}^{(k)}$ where $k = 1, \cdots, 4$ of the four detectors, which have ideal photon number resolution up to 2, 3, 4 and 5 photons for detectors 1, 2, 3, and 4, respectively. The heat map for the conditional probability matrix $\mathbf{\Pi}$ of the four-detector array is shown on the right for uniform splitting probabilities $\vec{c} = (1/4, 1/4, 1/4, 1/4)$, corresponding to $\vec{\tau} = (1/2, 1/\sqrt{3}, 1/\sqrt{2})$, demonstrating the improvement in photon number resolution with spatial multiplexing.

With this iterative method, given predetermined $\mathbf{\Pi}$ matrices of the detectors in the array, the number of terms to compute is linear in n and m. By leveraging the recursive structure of arrays, this approach is significantly more efficient than brute-force computation with Eq. 4.3 (see Methods).

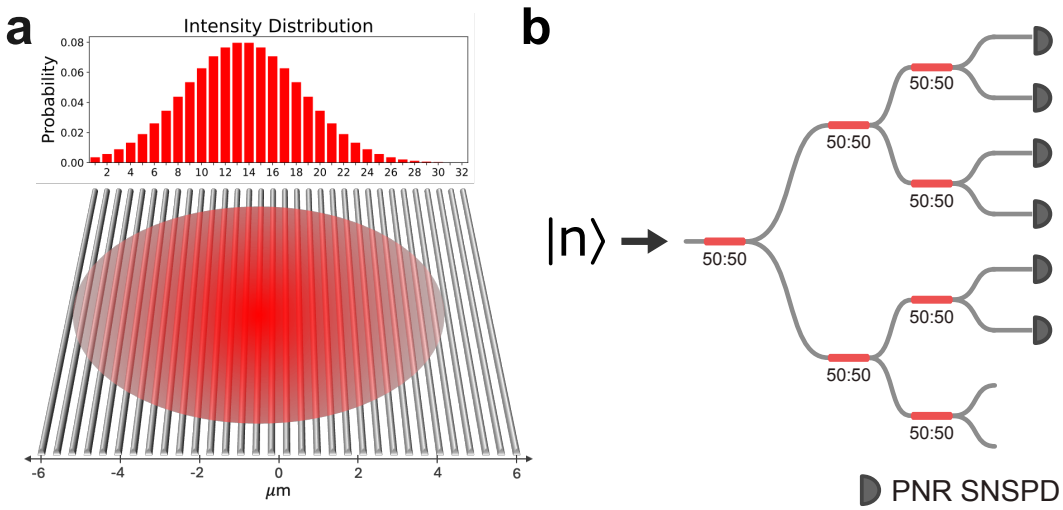

Figure 4.2: Array detector configurations for experimental detector tomography. a) Illustration of PEACOQ detector with the experimental Gaussian spatial mode of 1550 nm light coupled to 32 parallel nanowires. b) Illustration of splitting configuration for the spatially multiplexed array of six PNR SNSPDs.

4.3 Experimental detector tomography

We compare the models against experimentally reconstructed POVMs of two detector array configurations: (1) nonuniform spatial distribution across an array of 32 detectors, each without intrinsic PNR capability, and (2) uniform splitting distribution across array of six detectors, each with intrinsic PNR capability. For configuration 1, we use the PEACOQ detector, which is an array of 32 superconducting nanowires coupled to a single-mode SMF-28 telecommunications wavelength optical fiber [10]. The gaussian mode of the optical fiber is distributed across the linear array of nanowires (Fig. 4.2a), which enables pseudo-PNR through multiplexing, as well as faster photon counting than is possible with a single nanowire. For configuration 2, we use an array of six PNR SNSPDs, where input photons distributed uniformly across a optical fiber beamsplitter network (Fig. 4.2b).

To reconstruct the POVMs of the two detector configurations, we perform experimental detector tomography using the approach in Ref. [13]. For each configuration, counting statistics are acquired for various mean photon numbers of input coherent light pulses. The measured counting statistics can be related to the conditional probability matrix by expressing Eq. 4.1 as,

$$\mathbf{P} = \mathbf{F\Pi}, \tag{4.11}$$

where $\mathbf{P}$ is a $D \times N$ matrix containing the measured probabilities for N detector

outcomes over D probe states, $\mathbf{F}$ is $D \times M$ matrix that contains the photon number distributions of the D input states, each truncated at a maximum Hilbert space dimension M, and $\mathbf{\Pi}$ is the $M \times N$ conditional probability matrix of the detector, corresponding to the POVM elements in Eq. 4.2 with the sum truncated at $M - 1$. Each row of $\mathbf{P}$ corresponds to a histogram of the measurement outcome frequency for each mean photon number. For coherent states, each row of $\mathbf{F}$ is the computed Poisson distribution for each mean photon number. From known $\mathbf{P}$ and $\mathbf{F}$, $\mathbf{\Pi}$ is determined from matrix inversion with a CVXPY-based python module [13] using the code from [14].

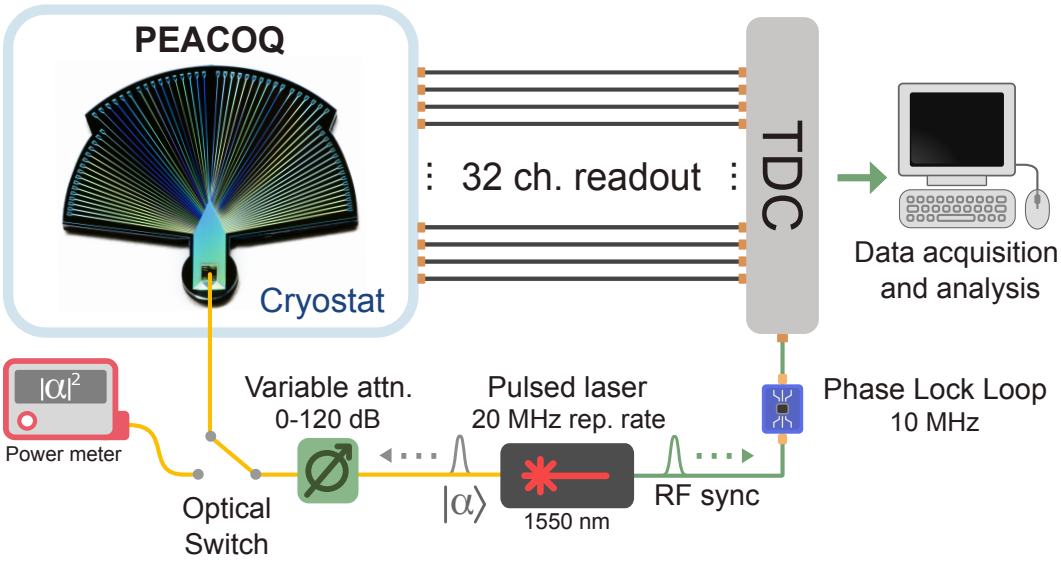

Figure 4.3: Experimental setup for tomography of the PEACOQ detector (pictured).

PEACOQ Detector

The experimental setup for tomography of the PEACOQ detector is shown in Fig. 4.3. The PEACOQ was measured in 0.9 K cryostat, in a modified version of Setup A as described in Ref. [10]. Figure 4.3 shows a schematic of the experimental setup. The ceramic ferrule of the optical fiber coupler was in direct contact with the detector chip. Each of the 32 channels is individually biased and read out. Three stages of amplifications, two of which were inside the cryostat at 40 K were used to amplify the pulses corresponding to photon detections. The pulses were then converted to time stamps using a custom 128-channel time-to-digital converter (TDC). The source of optical coherent states was a 1550 nm pulsed laser with a repetition rate of 20 MHz. Pulses from the laser passed through a variable attenuator, a polarization controller, and a switch before entering the cryostat. The switch sent

light to either the PEACOQ or a power meter, which was used to measure the mean photon number. The sync signal of the pulsed laser was converted to a 10 MHz signal using a phase-locked loop then sent to the TDC for synchronization.

Counting statistics are acquired at twelve attenuation settings corresponding to mean photon numbers ranging from $\mu = 0.4$ to 82. For each mean photon number, the time tags from each detector are accumulated over a duration of $\leq$ 1s, depending on the count rate. The time tags are binned to obtain the number of coincident clicks out the 32 detectors per pulse. The counting probabilities are constructed from the histogram of the number of the binned time tags, which is normalized to one and forms a row of the $\mathbf{P}$ matrix. Each row of the $\mathbf{F}$ matrix calculated from the Poisson distribution,

$$p_n(\mu) = \frac{\mu^n}{n} e^{-n}, \tag{4.12}$$

where n is truncated at $n = 124$ to fully capture the statistics for all probe states. The reconstructed $\mathbf{\Pi}$ is depicted in Fig. 4.4a up to $m = 25$ and $n = 50$.

We model the $\mathbf{\Pi}$ matrix using the iterative method, where each detector is assumed to be click detector with $\mathbf{\Pi}^{(k)}$ described by Eq. 4.4 for $k = 1$ to 32. The splitting probabilities $(c_1, ..., c_N)$ are obtained from the normalized intensity distribution depicted in Fig. 4.2a. To account for the detection efficiency of $\eta = 0.78$, a Bernoulli transformation is applied to the total $\mathbf{\Pi}$ matrix,

$$\mathbf{\Pi}^{(\eta)}_{mn} = \sum_{j=0}^{n} \mathbf{\Pi}_{mj} \binom{n}{j} \eta^j \, (1-\eta)^{n-j} \, . \tag{4.13}$$

The theoretical $\mathbf{\Pi}$ is depicted in Fig. 4.4b. The columns of the reconstructed and theoretical $\mathbf{\Pi}$ matrices are plotted in Fig. 4.4c and d, respectively. Despite discrepancies likely introduced by smoothing artifacts in the matrix inversion, both the reconstructed and modeled $\mathbf{\Pi}$ matrices reproduce the experimental counting probabilities (Fig. 4.4e). The predicted counting probabilities, calculated as $\mathbf{P} = \mathbf{F} \cdot \mathbf{\Pi}$ for the reconstructed and theoretical $\mathbf{\Pi}$ matrices are plotted in Figs. 4.4f and g, respectively. The solid curves are calculated from the Poisson distribution for each mean photon number, corresponding to counting probabilities measured with an ideal PNRD.

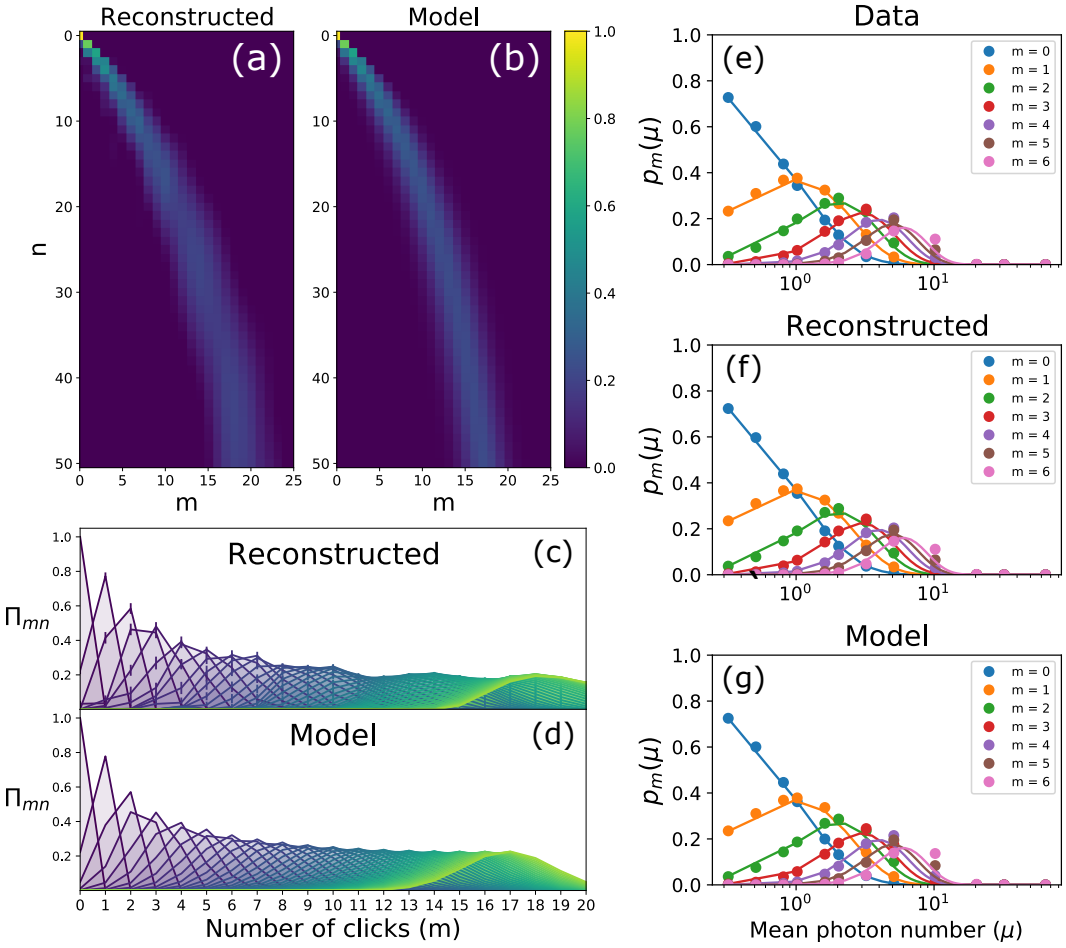

Figure 4.4: Heatmaps of a) reconstructed and b) theoretical $\mathbf{\Pi}$ matrices for the PEACOQ detector. The c) reconstructed and d) theoretical matrix elements $\mathbf{\Pi}_{\mathrm{m,n}}$ are plotted as a function of the measurement outcome $m = 0, \cdots, 32$ for $n = 0, \cdots, 50$. Each curve corresponds to a column of $\mathbf{\Pi}$. (e) Measured count probabilities $p_m(m)$ as a function of the mean photon number μ, for the first seven measurement outcomes $m = 0$ to 7. Reconstructed (f) and modeled (g) count probabilities as function of μ, calculated from the corresponding $\mathbf{\Pi}$ matrices. In (e)-(g), the detection efficiency is absorbed into the mean photon numbers.

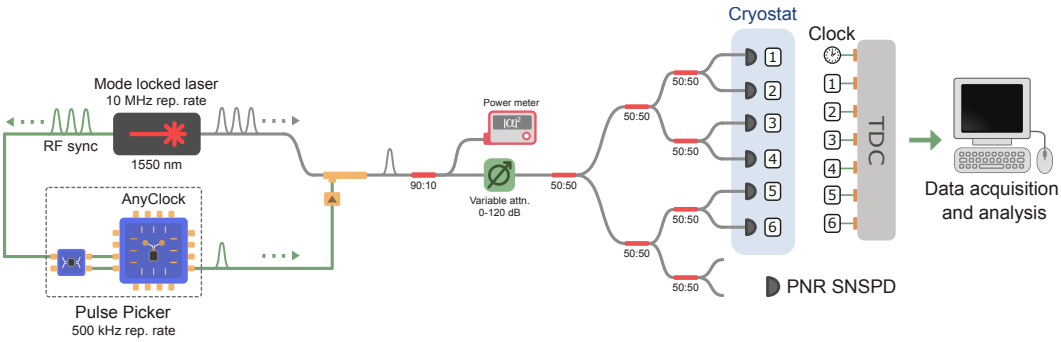

Figure 4.5: Experimental setup for detector tomography of spatially multiplexed PNR SNSPDs with uniform splitting distribution.

Spatially multiplexed PNR SNSPDs

The experimental setup for reconstruction of the POVM for an array of six PNR SNSPDs is shown in Fig. 4.5. We employ a mode-locked laser (Calmar) operating at a wavelength of 1550 nm with a repetition rate of 10 MHz. The emitted optical pulses have a temporal width of less than 2 ps and are directed to a high-extinction-ratio intensity modulator (extinction ratio > 40 dB). Simultaneously, the RF synchronization output from the laser is routed to a pulse picker module based on the Anyclock system (Skyworks, Si5344), which generates a 500 kHz RF signal. This output is passed through a digital delay generator (Stanford Research Systems, DG648) for precise temporal alignment with the optical pulse train. The delayed RF signal is amplified and used to drive the intensity modulator, selecting one out of every twenty optical pulses and reducing the repetition rate to 500 kHz. This downsampling avoids detector saturation and suppresses time-walk distortions in the SNSPD outputs at high count rates [15]. The modulator is carefully tuned to maximize extinction and minimize leakage from unpicked pulses. The modulated optical pulse train is passed through a 90:10 fiber splitter. The 90% output is used for optical power monitoring and serves as a clock reference for the time tagger. The remaining 10% is attenuated using variable optical attenuators (Yokogawa) and distributed to six superconducting nanowire single-photon detectors (SNSPDs) via a cascade of fiber beam splitters. Polarization controllers are placed before each detector to ensure optimal polarization alignment and coupling efficiency. The detectors, based on niobium nitride (NbN) nanowires, are housed in a Photonspot cryostat operating below 0.8 K. Detection signals are recorded using a Swabian Instruments Time Tagger X operated in standard mode for high-resolution time-correlated single-photon counting.

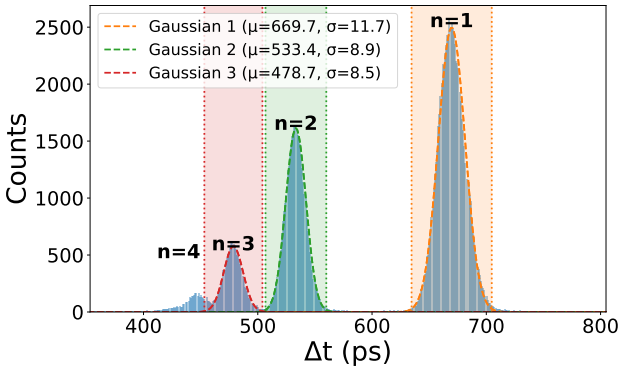

Figure 4.6: Histogram of time-tags accumulated over 10s for a mean photon number of ≈ 7 relative to the clock for the detector in channel 6. The windows for labeling time-tags with photon number are shown.

To reconstruct the POVMs of the individual detectors and the multiplexed detector array, time-tags are accumulated for a range of mean photon numbers of the input coherent light pulses. When multiple photons are incident on a single nanowire, multiple resistive hotspots are generated, which vary the amplitude and slew rate of the resulting RF output pulse. With a constant-threshold time-tagger, variations in slew rate translate into shifts in the registered time-tags [16]. This effect produces temporally distinguishable time-tag distributions for different numbers of incident photons. The histogram of time-tags accumulated over ten seconds is shown in Fig. 4.6 for one of the detectors, which can resolve up to four photons. The time-tags are assigned a photon number depending on the arrival time. To extract the range of arrival times associated with each photon number outcome, a Gaussian fit is performed on the first three time tag distributions, corresponding to $m = 1, 2$ and 3 photons. The arrival time windows for $m = 1, 2$ and 3 are extracted from $\pm 3\sigma$ from the mean of each distribution, depicted as the shaded regions in Fig. 4.6. Arrival times less than the -3σ of the $m = 3$ distribution are assigned $m = 4$. This procedure is performed for each detector in the array, with the windows for each detector held fixed across all measurements. For the multiplexed array of six detectors, each coincident event is assigned a total photon number equal to the sum of the individual photon numbers assigned to the time-tags registered by each detector.

The reconstructed $\mathbf{\Pi}^{(k)}$ for each detector ($k = 1, \cdots, 6$) are plotted in Fig. 4.7a-f. To isolate the PNR capability from the effects of optical loss, the detection efficiency is absorbed into the mean photon number for each detector. The reconstructed

and modeled $\mathbf{\Pi}$ for the detector array are plotted in Fig. 4.7g and h, respectively. For the model, we construct $\mathbf{\Pi}$ with the iterative procedure of Sec. 4.2 using the reconstructed $\mathbf{\Pi}^{(k)}$ of six detectors, assuming uniform splitting probabilities. The matrix elements for the reconstructed and modeled $\mathbf{\Pi}$ are compared for $n = 0, \cdots, 20$ in Figs. 4.7i-j. The counting probabilities from the reconstructed (Fig. 4.7l) and modeled (Fig. 4.7m) $\mathbf{\Pi}$ matrices reproduce the measured counting probabilities (Fig. 4.7k) for all mean photon numbers. The solid curves are calculated from Poisson statistics, corresponding to that measured with an ideal PNRD.

4.4 Discussion

We have developed a generalized theoretical framework for modeling POVMs of array detectors. We presented a model for $\mathbf{\Pi}$ (Eq. 4.3) that accommodates detectors with arbitrary POVM elements and arbitrary splitting probabilities across the array. We analyzed the computational complexity of computing $\mathbf{\Pi}_{mn}$ in various cases. For the case of click detectors, we found a closed-form solution for $\mathbf{\Pi}_{mn}$ that provides an exponential speedup over the multinomial representation. We then find an efficient construction of $\mathbf{\Pi}$ for a given set of detector POVMs and splitting probabilities. We take an iterative approach where individual POVMs are fused in pairs, taking advantage of the recursive structure of arrays. This allows us to model the POVMs of (1) the PEACOQ detector and (2) a spatially multiplexed array of PNR SNSPDs, corresponding to the cases of (1) 32 click detectors with Gaussian splitting probabilities and (2) six PNRDs with distinct POVMs and uniform splitting probabilities, respectively. We validate the models by perform experimental detector tomography of the PEACOQ detector and the multiplexed array of PNR SNSPDs, which demonstrate near ideal PNRD response for mean photon numbers up to $\mu \sim 10$ (see Methods). This work supports the development of PNRD arrays towards the goal of practical and near-ideal photon number discrimination for diverse photon counting applications.

4.5 Methods

Derivation of closed-form solution

Here we generalize the derivation for the 2N-port beamsplitter model of Paul et al. [9] to find a closed-form expression for $\mathbf{\Pi}^{m,n}$ for non-uniform distribution of photons across the output ports, with probabilities $\vec{c} = (c_1, c_2, ..., c_N)$. The $2N$-port beamsplitter has corresponding unitary U_N, which can be decomposed into 2×2 beamsplitters [17] for a given set of splitting probabilities. The $2N$-port beamsplitter

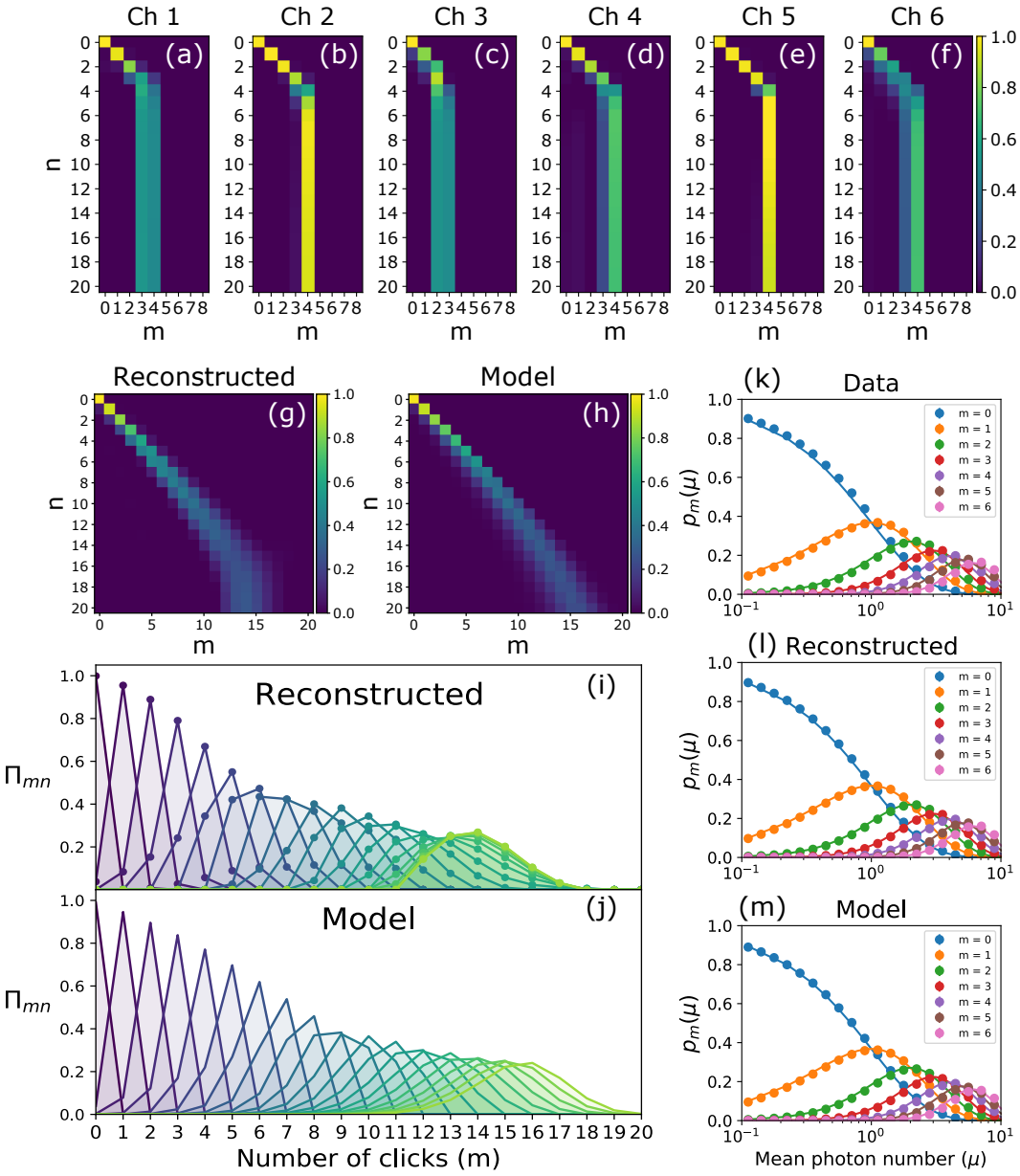

Figure 4.7: Heatmaps of reconstructed and theoretical $\mathbf{\Pi}$ matrices for the spatially multiplexed PNR SNSPDs configuration. (a)-(f) Heatmaps of reconstructed $\mathbf{\Pi}$ matrices for the Ch 1-6 detectors. Heatmaps of (g) reconstructed and (h) model $\mathbf{\Pi}$ matrices for the multiplexed array of Ch 1-6 detectors. Matrix elements for (i) reconstructed and (j) model $\mathbf{\Pi}$ matrices for the multiplexed array of Ch 1-6 detectors, where the curves ($n = 0 \cdots 20$) correspond to each column of $\mathbf{\Pi}$. (k) Measured count probabilities $p_m(m)$ as a function of the mean photon number μ, for the first seven measurement outcomes $m = 0$ to 7. Reconstructed (l) and modeled (m) count probabilities as function of μ, calculated from the corresponding $\mathbf{\Pi}$ matrices.

has the effect of sending a single photon at the first port into a superposition over the N output ports (see Fig. 4.1a),

$$\hat{a}_1^\dagger \xrightarrow{U_N} \sum_{i=1}^{N} \lambda_i \hat{b}_i^\dagger, \tag{4.14}$$

where λ_i is the amplitude for port i, $|\lambda_i|^2 = c_i$ is the probability that the photon is measured at port i, and $\sum_{i=1}^{N} c_i = 1$. Consider n photons incident to the first input port of the $2N$-port beamsplitter,

$$|n\rangle_1 |0\rangle_2 \cdots |0\rangle_N = \frac{1}{\sqrt{n!}} (\hat{a}_1^\dagger)^n |0\rangle \xrightarrow{U_N} \frac{1}{\sqrt{n!}} \left(\sum_{i=1}^{N} \lambda_i \hat{b}_i^\dagger \right)^n |0\rangle . \tag{4.15}$$

Applying the multinomial theorem, the RHS can be expanded as,

$$\left(\sum_{i=1}^{N} \lambda_i \hat{b}_i^\dagger \right)^n |0\rangle = \sum_{\sum j_i = n} \sqrt{\frac{n!}{j_1! \cdots j_N!}} (\lambda_1)^{j_1} \cdots (\lambda_N)^{j_N} |j_1\rangle \cdots |j_N\rangle , \tag{4.16}$$

where the sum is over all possible ways n photons can be distributed over the N wires.

Therefore, the probability of distributing n photons into j_1 photons at wire 1, j_2 photons at wire 2, ..., j_N photons at wire N is,

$$P_n(j_1, \cdots, j_N) = \frac{n!}{j_1! \dots j_N!} c_1^{j_1} \dots c_N^{j_N}, \tag{4.17}$$

where the probability of “on" outcomes on m wires is the sum of $P_n(j_1, \cdots, j_N)$ over m nonzero j's is,

$$\mathbf{\Pi}_{m,n} = \sum_{\sum j_i = n}^{(m)} P_n(j_1, \cdots, j_N) = \sum_{\sum j_i = n}^{(m)} \frac{n!}{j_1! j_2! \dots j_N!} c_1^{j_1} \dots c_N^{j_N}. \tag{4.18}$$

For the recursion relation in Eq. 4.7, the solution can be expressed in the more familiar form,

$$P(n, \mathbf{p}^{(m)}) = \sum_{i=0}^{m} (-1)^i \sum_{\mathbf{p}^{(m,i)}} \left(\sum_k p_k^{(m)} - \sum_k p_k^{(m,i)} \right)^n , \tag{4.19}$$

where $\mathbf{p}^{(m,i)}$ is the vector formed by taking a subset of i elements in $\mathbf{p}^{(m)}$; there are $\binom{m}{i}$ such vectors. The second sum in Eq. 4.19 is over all possible choices of $\mathbf{p}^{(m,i)}$.

In this form, it is clear that for $\mathbf{\Pi}_{m,n} = \sum_{\vec{c}^{(m)}} P(n, \vec{c}^{(m)})$ for the case of uniform splitting probabilities with $\vec{c}_k^{(m-i)} = 1/N$, Eq. 4.19 simplifies to expression from Ref. [9],

$$\mathbf{\Pi}_{mn} = \frac{1}{N^n}\binom{N}{m}\sum_{i=0}^{m}(-1)^i\binom{m}{i}(m-i)^n. \tag{4.20}$$

Plugging Eq. 4.19 into Eq. 4.6,

$$\mathbf{\Pi}_{mn} = \sum_{\mathbf{p}^{(m)}} P(n, \mathbf{p}^{(m)}) = \sum_{\mathbf{p}^{(m)}}\sum_{i=0}^{m}(-1)^i \sum_{\mathbf{p}^{(m,i)}}\left(\sum_k p_k^{(m)} - \sum_k p_k^{(m,i)}\right)^n \tag{4.21}$$

$$= \sum_{i=0}^{m}(-1)^i \sum_{\mathbf{p}^{(m)}}\sum_{\mathbf{p}^{(m,m-i)}}\left(\sum_k p_k^{(m,m-i)}\right)^n. \tag{4.22}$$

We can further simplify the solution. Two of the sums can be combined due to redundancy,

$$\sum_{\mathbf{p}^{(m)}}\sum_{\mathbf{p}^{(m,m-i)}}\left(\sum_k p_k^{(m,m-i)}\right)^n = \frac{\binom{N}{m}\binom{m}{i}}{\binom{N}{m-i}}\sum_{\mathbf{p}^{(m-i)}}\left(\sum_k p_k^{(m-i)}\right)^n. \tag{4.23}$$

yielding the expression in Eq. 4.8,

$$\mathbf{\Pi}_{mn} = \binom{N}{m}\sum_{i=0}^{m}(-1)^i\frac{\binom{m}{i}}{\binom{N}{m-i}}\sum_{\mathbf{p}^{(m-i)}}\left(\sum_k p_k^{(m-i)}\right)^n.$$

Iterative construction of the POVM elements

For an array of N detectors, each with a set of POVM elements, which are described the matrix $\mathbf{\Pi}^{(j)}$ for the jth detector, the splitting probabilities $(c_1, \cdots, c_N)$ can be mapped to transmittances of a $2N$-port beamsplitter (see Fig. 4.8) as,

$$\hat{a}_{\text{in}} \xrightarrow{U_N} \tau_1\hat{a}_1 + r_1\tau_2\hat{a}_2 + ... + (r_1\cdots r_{N-1}\tau_{N-1})\hat{a}_{N-1} + (r_1\cdots r_{N-1})\hat{a}_N, \tag{4.24}$$

where $|r_n|^2 = 1 - |\tau_n|^2$ for $n \in [1, N-1]$. The splitting probabilities are related to the transmittances as,

$$c_n = \begin{cases} |r_1|^2\cdots|r_{N-1}|^2, & \text{for } n = 1, \\ |\tau_n|^2(|r_1|^2\cdots|r_{n-1}|^2), & \text{for } 1 < n < N, \\ |\tau_1|^2, & \text{for } n = N, \end{cases} \tag{4.25}$$

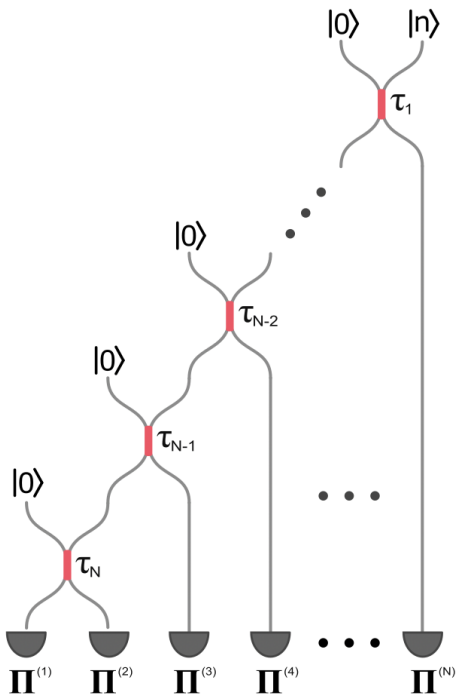

Figure 4.8: Setup for the iterative construction of the POVM elements for an array of N detectors.

satisfying $\sum_{j=1}^{N} c_j = 1$. Therefore, given a set of a splitting probabilities $\vec{c} = (c_1, ..., c_N)$, the transmittances (neglecting phase) can be computed recursively as,

$$|\tau_1|^2 = c_N, \qquad |\tau_n|^2 = \frac{c_{N-(n-1)}}{(1-|\tau_1|^2)\cdots(1-|\tau_{n-1}|^2)} \quad \text{for } 1 < n < N. \tag{4.26}$$

After computing the transmittances, the conditional probability matrix elements can be computed recursively using Eq. 4.10 as,

$$\mathbf{\Pi}^{(1,2)}_{m,n} = \sum_{i=0}^{m}\sum_{j=0}^{n}\binom{n}{j}(|\tau_N|^2)^j(1-|\tau_N|^2)^{n-j}\mathbf{\Pi}^{(1)}_{i,j}\mathbf{\Pi}^{(2)}_{m-i,n-j}, \tag{4.27}$$

$$\mathbf{\Pi}^{(1,2,3)}_{m,n} = \sum_{i=0}^{m}\sum_{j=0}^{n}\binom{n}{j}(|\tau_{N-1}|^2)^j(1-|\tau_{N-1}|^2)^{n-j}\mathbf{\Pi}^{(1,2)}_{i,j}\mathbf{\Pi}^{(3)}_{m-i,n-j}, \tag{4.28}$$

$$\vdots \tag{4.29}$$

$$\mathbf{\Pi}^{(1,\cdots,N)}_{m,n} = \sum_{i=0}^{m}\sum_{j=0}^{n}\binom{n}{j}(|\tau_1|^2)^j(1-|\tau_1|^2)^{n-j}\mathbf{\Pi}^{(1,\cdots,N-1)}_{i,j}\mathbf{\Pi}^{(N)}_{m-i,n-j}, \tag{4.30}$$

where $\mathbf{\Pi}^{(1,\cdots,k)}$ is the conditional probability matrix for an array comprised of detector 1 through k, where $k \in 1, \cdots, N$, and $\mathbf{\Pi} = \mathbf{\Pi}^{(1,\cdots,N)}$ is the conditional probability matrix of the entire array of N detectors.

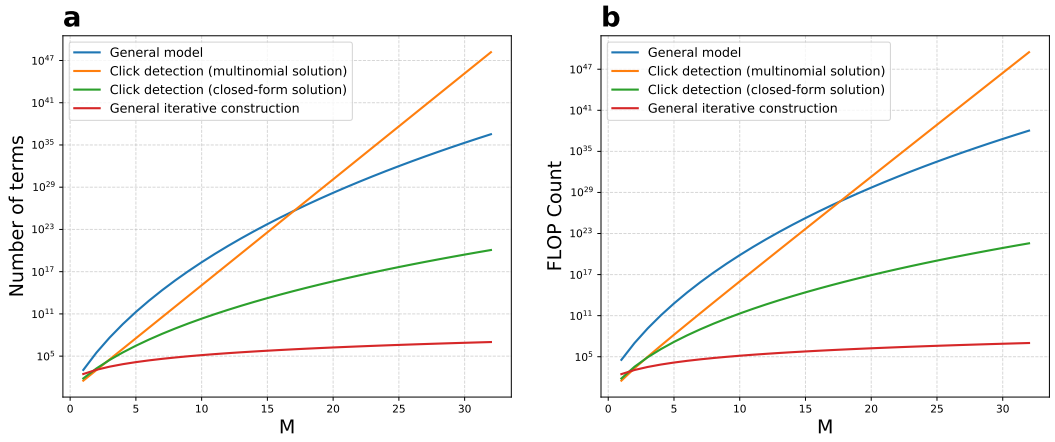

Figure 4.9: Computational complexity as a function of conditional probability matrix ($\mathbf{\Pi}$) size. a) Number of terms to calculate and b) estimated number of FLOP counts for the general model (Eq. 4.3), the multinomial solution for the click detection model (Eq. 4.5), the closed-form solution for the click detection model (Eq. 4.8), and the generalized iterative construction for computing a conditional probability matrix $\mathbf{\Pi}$ of dimensions $M \times M$.

Computational complexity

The number of terms in each expression directly affects the computational complexity of evaluating $\mathbf{\Pi}$, since each term corresponds to a unique combination of photon distributions and detector responses that must be explicitly computed. In the computation of $\mathbf{\Pi}_{mn}$, each term incurs a number of floating-point operations (FLOPs), such as exponentiations, multiplications, and factorial evaluations, where the total FLOP count is a proxy for runtime. The total FLOP count is a widely used metric for estimating algorithmic efficiency, particularly in numerical linear algebra and scientific computing, where it serves as a hardware-agnostic measure of computational cost [18]. The number of terms and estimated FLOP count for Eq. 4.3, Eq. 4.5, Eq. 4.8, and the iterative method are summarized in Table 4.1. For each equation, the number of terms and estimated FLOP counts for computing a $\mathbf{\Pi}$ matrix of size $M \times M$ are plotted in Fig. 4.9 as a function of M for an array size of $N = 32$. The general model Eq. 4.3 and multinomial expression Eq. 4.5 quickly become intractable even for models values of $M \geq 10$. The closed-form solution in Eq. 4.8 provides a improvement for the click detection case with roughly polynomial scaling in M, but still becomes intractable for modest values of M. The iterative method is the most efficient, with scaling $O(M^2)$.

Method	Term count	FLOPs per term	Total FLOPs
General model (Eq. 4.3)	$\binom{m+N-1}{N-1}\binom{n+N-1}{N-1}$	$O(N)$	$O\left(N\binom{m+N-1}{N-1}\binom{n+N-1}{N-1}\right)$
Multinomial solution (Eq. 4.5)	$\binom{N}{m}\, S(n,m)\, m!$	$O(m)$	$O\left(m\binom{N}{m}S(n,m)m!\right)$
Closed-form solution (Eq. 4.8)	$\sum_{i=0}^{m}\binom{m}{i}\binom{N}{m-i}$	$O(m)$	$O\left(m\sum_{i=0}^{m}\binom{m}{i}\binom{N}{m-i}\right)$
Iterative construction	$N(m+1)(n+1)$	$O(1)$	$O(N(m+1)(n+1))$

Table 4.1: Computational complexity of computing the matrix elements $\mathbf{\Pi}_{mn}$ for the different approaches and configurations. FLOPs per term estimate the number of operations per term including binomial coefficients and multiplications.

Count fidelity

We evaluate the performance of the detector arrays for the given probe states with the count fidelity,

$$F = \left(\sum_n \sqrt{p_n q_n}\right)^2, \tag{4.31}$$

which quantifies how near the measured count distribution ($\{p_n\}$) match the true photon number distribution ($\{q_n\}$) of the probe states. The fidelities for the PEACOQ detector and the PNR SNSPD array detector are plotted in Fig. 4.10 as a function of mean photon number. Both detectors exhibit $\geq 90\%$ count fidelities for coherent states with up to $\mu \sim 10$.

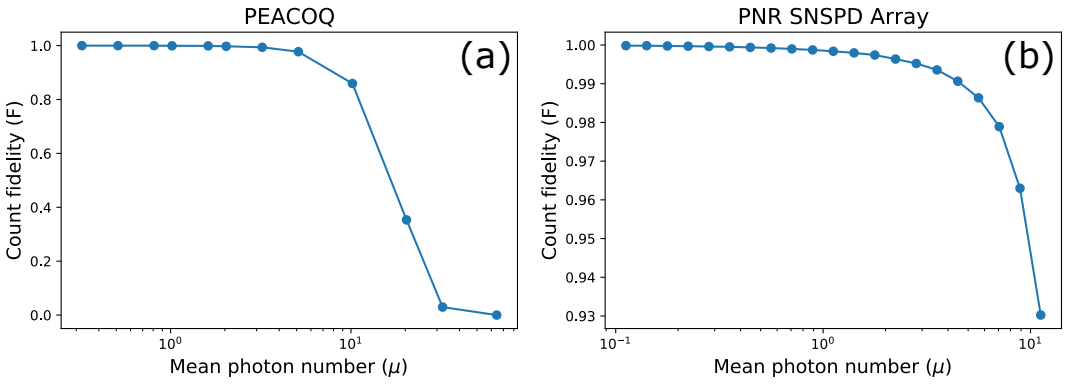

Figure 4.10: Count fidelities for a) the PEACOQ detector and b) the array of six PNR SNSPDs.

References

[1] Aleksander Divochiy, Francesco Marsili, David Bitauld, Alessandro Gaggero, Roberto Leoni, Francesco Mattioli, Alexander Korneev, Vitaliy Seleznev, Nataliya Kaurova, Olga Minaeva, et al. "Superconducting nanowire photon-number-resolving detector at telecommunication wavelengths." In: Nature Photonics 2.5 (2008), pp. 302–306.

[2] F. Marsili, D. Bitauld, A. Gaggero, S. Jahanmirinejad, R. Leoni, F. Mattioli, and A. Fiore. "Physics and application of photon number resolving detectors based on superconducting parallel nanowires." In: New Journal of Physics 11.4 (2009), p. 045022.

[3] Di Zhu, Qing-Yuan Zhao, Hyeongrak Choi, Tsung-Ju Lu, Andrew E. Dane, Dirk Englund, and Karl K. Berggren. "A scalable multi-photon coincidence detector based on superconducting nanowires." In: Nature Nanotechnology 13.7 (2018), pp. 596–601.

[4] M. J. Fitch, B. C. Jacobs, T. B. Pittman, and J. D. Franson. "Photon-number resolution using time-multiplexed single-photon detectors." In: Physical Review A 68 (2003), p. 043814. DOI: 10.1103/PhysRevA.68.043814.

[5] Daryl Achilles, Christine Silberhorn, Cezary Sliwa, Konrad Banaszek, Ian A. Walmsley, Michael J. Fitch, Bryan C. Jacobs, Todd B. Pittman, and James D Franson. "Photon-number-resolving detection using time-multiplexing." In: Journal of Modern Optics 51.9-10 (2004), pp. 1499–1515.

[6] Fadri Grünenfelder, Alberto Boaron, Giovanni V Resta, Matthieu Perrenoud, Davide Rusca, Claudio Barreiro, Raphaël Houlmann, Rebecka Sax, Lorenzo Stasi, Sylvain El-Khoury, et al. "Fast single-photon detectors and real-time key distillation enable high secret-key-rate quantum key distribution systems." In: Nature Photonics 17.5 (2023), pp. 422–426.

[7] Rajveer Nehra, Chun-Hung Chang, Qianhuan Yu, Andreas Beling, and Olivier Pfister. "Photon-number-resolving segmented detectors based on single-photon avalanche-photodiodes." In: Optics Express 28.3 (2020), pp. 3660–3675.

[8] Timon Schapeler, Jan Philipp Höpker, and Tim J Bartley. "Quantum detector tomography of a 2× 2 multi-pixel array of superconducting nanowire single photon detectors." In: Optics Express 28.22 (2020), pp. 33035–33043.

[9] H. Paul, P. Törmä, T. Kiss, and I. Jex. "Photon chopping: new way to measure the quantum state of light." In: Physical Review Letters 76.14 (1996), p. 2464.

[10] Ioana Craiciu, Boris Korzh, Andrew D. Beyer, Andrew Mueller, Jason P. Allmaras, Lautaro Narváez, Maria Spiropulu, Bruce Bumble, Thomas Lehner, Emma E. Wollman, et al. "High-speed detection of 1550 nm single photons with superconducting nanowire detectors." In: Optica 10.2 (2023), pp. 183–190.

[11] Lorenzo Stasi, Gaëtan Gras, Riad Berrazouane, Matthieu Perrenoud, Hugo Zbinden, and Félix Bussières. "Fast high-efficiency photon-number-resolving parallel superconducting nanowire single-photon detector." In: Physical Review Applied 19.6 (2023), p. 064041.

[12] Adriana E. Lita, Aaron J. Miller, and Sae Woo Nam. “Counting near-infrared single-photons with 95% efficiency.” In: Optics Express 16.5 (2008), pp. 3032–3040.

[13] Timon Schapeler, Jan Philipp Höpker, and Tim J. Bartley. “Quantum detector tomography of a 2× 2 multi-pixel array of superconducting nanowire single photon detectors.” In: Optics Express 28.22 (2020), pp. 33035–33043.

[14] Timon Schapeler. Detector Tomography Python Code. https://physik.uni-paderborn.de/en/mesoscopic-quantum-optics/resources/downloads. 2020.

[15] Andrew Mueller, Emma E. Wollman, Boris Korzh, Andrew D. Beyer, Lautaro Narvaez, Ryan Rogalin, Maria Spiropulu, and Matthew D. Shaw. “Time-walk and jitter correction in SNSPDs at high count rates.” In: Applied Physics Letters 122.4 (Jan. 2023), p. 044001. DOI: 10.1063/5.0129147.

[16] Samantha I. Davis, Andrew Mueller, Raju Valivarthi, Nikolai Lauk, Lautaro Narvaez, Boris Korzh, Andrew D. Beyer, Olmo Cerri, Marco Colangelo, Karl K. Berggren, et al. “Improved heralded single-photon source with a photon-number-resolving superconducting nanowire detector.” In: Physical Review Applied 18.6 (2022), p. 064007.

[17] Michael Reck, Anton Zeilinger, Herbert J. Bernstein, and Philip Bertani. “Experimental realization of any discrete unitary operator.” In: Phys. Rev. Lett. 73 (1 July 1994), pp. 58–61.

[18] Gene H. Golub and Charles F. Van Loan. Matrix Computations. 4th. Johns Hopkins University Press, 2013.